Transport in Porous Media manuscript No.
(will be inserted by the editor)

Validity of capillary imbibition models in paper-based microfluidic applications

Gabriel S. Gerlero · Andrés R. Valdez · Raúl Urteaga · Pablo A. Kler

Abstract Paper-based microfluidics has grown continuously over the last few years. One of the most important characteristics of paper-based microfluidic devices is the ability to pump fluids with the single action of capillary forces. However, fluid flow control in paper-based microfluidic devices has been studied primarily through empirical approaches; and as paper-based microfluidic devices have become more complex, more general and precise models of fluid flow are required. Particularly difficult to model are unsaturated flow conditions, which are critical to the overall performance of paper-based analytical devices, which may contain pre-adsorbed reagents such as indicator particles or antibodies. In this work we propose an objective test and a discussion on the suitability of different models (including a novel model derived here from LET-based models) that represent fluid imbibition dynamics in paper substrates. We reproduce experimental fluid fronts with the best parameter fits of the different models to show their actual capabilities to represent the moisture content function and present an analysis of propagation of uncertainties to obtain a final objective quantification of the quality of model fits. This objective analysis will endow the paper-based microfluidics community with objective information about modeling tools to improve the designs and performance of these devices.

Keywords Unsaturated flow · Paper based microfluidics · Imbibition models · Boltzmann transformation · Whatman filter paper

Gabriel S. Gerlero · Pablo A. Kler
Centro de Investigación en Métodos Computacionales (CIMEC, UNL–CONICET). Colectora RN 168 Km 472, S3000GLN Santa Fe, Argentina.

Andrés R. Valdez
Computational Modeling Graduate Program. Federal University of Juiz de Fora, Juiz de Fora, MG, Brazil.

Raúl Urteaga
Instituto de Física del Litoral (IFIS Litoral, UNL–CONICET).
Güemes 3450, S3000GLN Santa Fe, Argentina.

Pablo A. Kler
Departamento de Ingeniería en Sistemas de Información, FRSF-UTN.
Lavaise 610, S3004EWB Santa Fe, Argentina. E-mail: kler@cimec.unl.edu.ar

1 Introduction

Paper-based microfluidics has grown continuously over the last decade, mainly due to its capabilities for the implementation of portable chemical and biochemical assays (Salentijn et al., 2018). The advantages offered by paper-based analytical devices have been extensively reported in the literature (Ozer et al., 2020), yet they may be summarized as: low costs of manufacturing, transport, operation (due to small reactant volumes), and final disposal; along with compatibility with different detection methods (sometimes involving mobile devices (Hassan et al., 2020)) that make them easy-to-use by untrained personnel (Kim et al., 2020). The most important and attractive of all the characteristics of paper-based microfluidic devices is the ability to pump fluids without any external power supply, with the single action of capillary forces due to the wicking nature of cellulose fibers (Modha et al., 2021). Capillary flow in paper-based microfluidic devices has been exploited since the first works at the beginning of 20^{th} century (Yetisen et al., 2013), later on with the widespread use of lateral flow assays (Berli and Kler, 2016), and recently in more complex applications (Mora et al., 2019). Especially when considering these recent developments that involve complex multi-layer, multi-step, experimental layouts (Schaumburg and Berli, 2019), an accurate and precise control of the fluid flow is critical.

Unfortunately, fluid flow control in paper-based microfluidic devices has been studied mainly through empirical approaches due to the following two reasons (Franck et al., 2021): (i) as mentioned before, manufacturing processes are affordable, and multiple experiments with different layouts and operational conditions can be conducted simultaneously within reasonable timeframes (Yamada et al., 2017); and (ii), as far as paper is an intricate porous structure of intertwined fibers, predictions of flow behaviors are particularly challenging and, presently, no robust and validated mathematical models are available (Schaumburg et al., 2018b). This empirical approach has certainly been effective for lateral flow assay configurations and simple devices, but as paper-based microfluidic devices have become more complex, more general and precise models of fluid flow are required (Lim et al., 2019).

At this point, we can discriminate between saturated and unsaturated flow conditions. It is frequent in the paper-based microfluidics community to employ simplified mathematical models of devices operating under saturated flow conditions, i.e. when all the operational domain of the device is completely wet (Schaumburg et al., 2018a). When saturated flow conditions are assumed, Darcy's Law is sufficient for modeling the flow, with the permeability remaining constant, only pressure boundary conditions are enough to obtain a valid solution for the velocity field (Gerlero et al., 2021). However, considering a fully saturated domain precludes the local effects of capillarity. Moreover, unsaturated flow conditions are those that are actually critical for the analytical performance of paper-based devices in general, which in many practical cases contain pre-adsorbed reactants such as reporter particles or antibodies (among others) that are transported by the infiltrating fluid front (Rath and Toley, 2020).

Unsaturated flow conditions during imbibition processes are extremely complex and were initially studied by using models based on the Lucas–Washburn Equation (Elizalde et al., 2016; Pan et al., 2021). Such models are appropriate to determine the position of the wetting front in an averaged manner in the presence

of one-dimensional infiltration, but are not capable at all of describing the observable shapes of such fronts, nor can they be applied in two- or three-dimensional domains (Bear and Cheng, 2010). In order to precisely describe fluid fronts during imbibition processes, the dependence of capillary pressure and permeability with saturation must be adequately accounted for (Santagata et al., 2020). It is worth noting that it is not only saturation that is important for these applications: the flow velocity field, itself obtained from derivatives of saturation, enables further modeling of scalar transport with convection–diffusion–reaction equations (Gamazo et al., 2016), crucial for the design of paper-based microfluidic analytical devices.

The Richards Equation (Richards, 1931) is the most accepted for describing fluid flow in unsaturated porous media (Hertaeg et al., 2020). When paper-based microfluidic devices are considered, a special case of the Richards Equation occurs in which gravity can be neglected (due to the usual positioning of devices and/or the negligible effect of gravity verified through the extremely low Bond numbers and extremely large wetting lengths (Das and Mitra, 2013). For spontaneous capillary flow, we can reduce the Richards Equation in terms of the volumetric moisture content (θ) to obtain:

$$\frac{\partial \theta}{\partial t} = \nabla \cdot (D(\theta) \nabla \theta) \,. \tag{1}$$

This equation is known as the moisture diffusivity equation, and the key condition for the success of this equation as a valid model for imbibition flow is the moisture diffusivity function $D(\theta)$ (Bear and Cheng, 2010). Hydraulic models for $D(\theta)$ such as those by Brooks and Corey (1964) and by Van Genuchten (1980) provide parametrized closed-form expressions for such function. Details about these models can be found on their original works cited here as well as in the supporting information for this paper.

Adequately solving eq. 1 can provide an outstanding tool for sensible improvements on the design of complex paper-based microfluidic devices. The success of this numerical process is subject to the usage of a robust and correct model for $D(\theta)$ and the implementation of an efficient numerical tool for solving eq. 1 with different $D(\theta)$ functions. When defining a robust and correct model for $D(\theta)$, it is important to mention here that the most recognized models (the already mentioned Brooks and Corey (1964) and Van Genuchten (1980) models) were originally developed considering common soil components (e.g. sand, rocks, clay) as substrates. Clearly, the microscopic structure of paper differs from these soil components, so that special considerations may need to be made in order to obtain adequate results from such models. A limited amount of work has been done trying to characterize paper substrates by following these classical soil-oriented models, without reaching consistent and reproducible results (Perez-Cruz et al., 2017; Rath et al., 2018; Rath and Toley, 2020). The same situation occurred when using other alternative models (Cummins et al., 2017; Ruoff et al., 1959, 1960; Philip, 1955). An objective test of the suitability of these models for paper-based microfluidic applications is still missing (Terzis et al., 2018).

More recently, an alternative set of correlations has been presented by Lomeland et al. (2005). These phenomenologically driven models with the name “LET” are targeted towards multiphase fluid flow in soils as well, but also particularly

for applications in enhanced oil recovery (Lomeland and Ebeltoft, 2008; Lomeland, 2018). The large amount of parameters present in the LET models allows for simplifications to produce a new model with fewer parameters compatible with paper-based microfluidic applications. We introduce here a model based on such simplification called "LETd", whose mathematical foundations can be found in the next section.

In this work, we propose objective testing and a discussion on the suitability of different contemporary $D(\theta)$ models for representing the fluid flow imbibition dynamics in paper substrates. First, we conducted careful experiments to obtain an accurate measure of the imbibition process under controlled conditions. Then, we attempt reproduce these experimental fluid fronts by finding the best parameter fits of the models, showing the actual capabilities of each model to represent the moisture content function $\theta(x,t)$ as a function of space and time. Additionally, an experimental data–driven reconstruction of the $D(\theta)$ function is presented and compared with the $D(\theta)$ function obtained for each model, providing more information about the suitability of the methods for the whole range of θ and the correctness of the assumptions made for the LETd model. Afterwards, we present an analysis on the propagation of uncertainties to characterize the robustness of the models in representing the experimental data under different experimental conditions, and finally we provide an objective quantification of the effect of such uncertainties in the quality of the model fit through an exhaustive (local) error estimation.

Experimental conditions to match the most frequently used in paper-based microfluidics—lateral flow in Whatman No. 1 paper—were chosen. The main result of this work is the confirmation that the LETd model can effectively represent fluid flow imbibition front in the whole range of θ, obtaining more consistent results when compared with classical models, but also offering a more suitable mathematical expression for further modeling of capillary imbibition in more complex domains, including use of the flow velocity field for coupled scalar transport problems. Through this confirmation, the paper-based microfluidics community has new tools to improve designs of contemporary devices as well as to adequately face new challenges in this key technology field.

2 Mathematical background

2.1 Mathematical description of lateral flow.

For our model problem, we adopt lateral flow conditions[1] in an unsaturated flow problem governed by eq. 1 as follows: for any coordinate x defined on a semi-infinite one-dimensional spatial domain $(0,\infty)$, find for any instant t in the temporal domain $[0,\infty)$ the moisture content profile $\theta := (x,t) \mapsto \mathbb{R}$ that satisfies the

[1] The set of physicochemical hypotheses of this model is described in the supporting information.

initial–boundary value problem:

$$\begin{cases} \dfrac{\partial\theta}{\partial t} = \dfrac{\partial}{\partial x}\left(D(\theta)\dfrac{\partial\theta}{\partial x}\right), & \text{in } (0,\infty)\times[0,\infty), \\ \theta-\theta_i = 0, & \text{on } t=0, \quad \text{for any } x\in(0,\infty), \\ \theta-\theta_b = 0, & \text{on } x=0, \quad \text{for any } t\in[0,\infty). \end{cases} \tag{2}$$

By considering θ_i as the initial moisture content and θ_b equal to the porosity θ_s, this problem models the imbibition of a rectangular strip of material in contact with liquid at $x = 0$, i.e. the configuration known as lateral flow in paper-based microfluidics. In practice, θ_b cannot be exactly equal to θ_s because the expressions used for $D(\theta)$ are usually singular at $\theta = \theta_s$ (Bear and Cheng, 2010). Hence, $\theta_b = \theta_s - \epsilon$ with $\epsilon = 1\times10^{-7}$.

2.2 Boltzmann transformation.

A convenient property of eq. 2 is that its solutions are self-similar, and the problem as a whole is susceptible to a similarity transformation known as the Boltzmann transformation (Boltzmann, 1894; Bear and Cheng, 2010). The transformation means that a solution θ, which is a function of x and t, can also be expressed in terms of a single new variable ϕ—known as the Boltzmann variable—instead, defined as:

$$\phi = \frac{x}{\sqrt{t}}. \tag{3}$$

The Boltzmann transformation is useful in many ways. First, it can be applied to experimental observations of lateral flow to reduce the dimensionality of the data. Furthermore, it serves as a verification that eq. 1 is sufficient for a thorough description of unsaturated flow in the studied material. Finally, it can be leveraged to solve eq 2 more easily, as it is the case with the numerical tool purposely selected for our analysis (Gerlero et al., 2020).

An additional property of the Boltzmann transformation is that it allows one to obtain $D(\theta)$ from a known differentiable solution to eq. 2 via the integral expression, effectively solving the inverse problem:

$$D(\theta) = -\frac{1}{2}\frac{d\phi}{d\theta}\int_{\theta_i}^{\theta}\phi\,d\theta. \tag{4}$$

This method was first proposed for fluid flow in porous media by Bruce and Klute (1956) and is known as Boltzmann–Matano analysis in the general study of diffusion (Tumidajski and Chan, 1996). It must be noted that the use of this method alone to solve an inverse problem is generally limited in precision when θ is known as discrete experimental data (Bruce and Klute, 1956; Cummins et al., 2017) unless the solution is also approximated with an closed-form expression (Espejo et al., 2014; Evangelides et al., 2010, 2005).

2.3 Description of the LETd model

Based on the LET family of correlations for special core analysis (Lomeland, 2018), we propose a similar expression to approximate the experimental diffusivity. We define the LETd model as:

$$D(\theta) = D_{wt}\frac{S_{wp}^{L}}{S_{wp}^{L} + E(1 - S_{wp})^{T}}, \tag{5}$$

where $S_{wp} = \frac{S_w - S_{wir}}{1 - S_{wir}} = \frac{\theta - \theta_s S_{wir}}{\theta_s - \theta_s S_{wir}}$. D_{wt} (re-scaling factor), L, E, T and S_{wir} are parameters in the LETd model and S_w is defined as the moisture content divided by the material's porosity (see the supporting information for more details).

3 Materials and methods

3.1 Imbibition experiments

Measurement of initial moisture content. Solving eq. 2 requires one to know the initial condition in the medium. The initial moisture content in the paper can be estimated by comparing the air-dry and oven-dry weights of the material. For this, paper discs of Whatman No. 1 paper (Whatman grade No. 1, 120 mm discs, Cityva, Marlborough, USA) were initially weighed in ambient conditions. Afterwards, the discs were heated in an oven (KO-30CRS, Buenos Aires, Argentina) at 105 °C. The paper was left to dry overnight and weighed again immediately following removal from the oven. Finally, the discs were weighed once again after 24 hours of being left under ambient conditions.

Lateral flow experiments. Paper-based devices were fabricated using craft-cutting and hot lamination (DASA LM330, DASA SRL, Buenos Aires, Argentina). Rectangular (30 mm × 10 mm) strips of Whatman No. 1 paper were cut along the machine direction. Paper strips were laminated in film pouches (150 µm thick, Binderplus, Santa Fe, Argentina) at 135 °C, at a speed of 3.5 mm s^{-1}. A small section 3 mm in length was left exposed on one side to act as the reservoir for the imbibition. When comparing this lamination strategy with similar setups based on wax printing, the former provides remarkably higher stability for the fluid front flow, avoiding distortions in the shape of the front caused by the hydrophobic boundaries created in wax-printed channels; as discussed, for example, by Hong and Kim (2015).

The devices were placed horizontally on a surface illuminated with a white backlighting LED panel akin to the one used by Urteaga et al. (2018). Transmitted light was captured from above by using a high-resolution digital camera (Canon EOS Rebel T5, Canon Inc., Tokyo, Japan) connected to a PC. The camera was positioned vertically 20 cm over the surface and manually focused. Images of the strips with a spatial resolution of about 20 µm per pixel were captured in intervals of 5 seconds.

Deionized water (from an inverse osmosis purifier Osmoion, Apema SRL, Villa Domínico, Argentina) was then deposited on the reservoir of each strip. We took

note of the time of start of imbibition on each device to the nearest half second. The devices were then left untouched until the steady state was reached with the paper fully saturated everywhere. In all cases, the first image was captured 5 seconds after the start of imbibition. This time is considerably larger than the timescale involved in the early imbibition regimes reported in the literature (Das et al., 2012); consequently, such regimes are excluded from the analysis.

Figure 1**A** shows a diagram of the paper-based devices and experimental setup used for the imbibition experiments. Figure 1**B** is a composite of images captured during the imbibition of a strip—each 5 seconds apart—, where the effect of moisture content on light transmission can be observed.

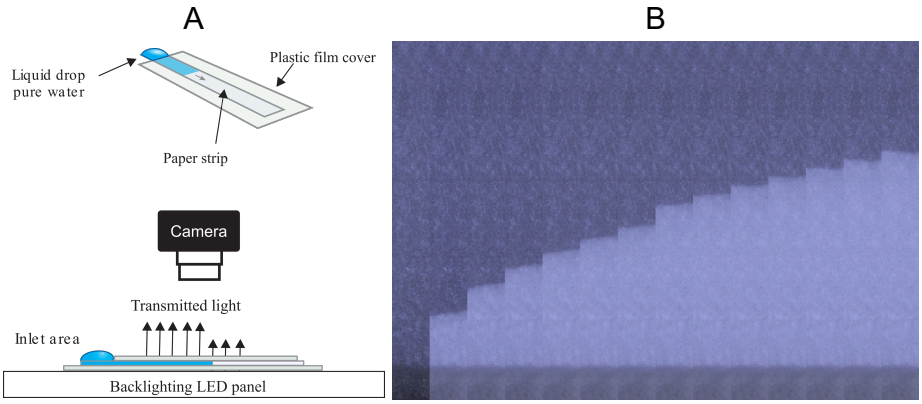

Fig. 1 **A** Diagram of the paper-based devices and experimental setup for the lateral flow experiments. **B** Sequence of images captured during imbibition of single device (images are cropped in width).

Porosity measurements To estimate the porosity, the paper-based devices used in the lateral flow experiments were weighed both before the imbibition and immediately after the experiments—i.e., when still fully saturated and after carefully drying the leftover water in the reservoirs.

Data processing of lateral flow experiments We developed a Python program to analyze the images and extract the equivalent water content profile. To approximate the distribution in moisture content in each strip, we assume a linear relationship between a normalized intensity of transmitted light $\tilde{Y}$ and water uptake in the paper (Urteaga et al., 2019; Vincent et al., 2017). The experimentally observed moisture content can then be expressed as:

$$\theta^{exp} = \theta_i + (\theta_s - \theta_i)\tilde{Y}, \tag{6}$$

so that $\tilde{Y} = 0$ at air-dry conditions ($\theta = \theta_i$) and $\tilde{Y} = 1$ when the paper is fully saturated with water ($\theta = \theta_s$). $\tilde{Y}$ is further defined as:

$$\tilde{Y} = \frac{Y - Y_i}{Y_s - Y_i}, \tag{7}$$

where Y represents the intensity of each pixel on the strip as captured in a certain image, Y_i the intensity of that same point in the initial condition, and Y_s is the intensity when fully saturated. All these values are previously normalized by the average intensity of a strip that remains always dry to control any change in ambient lighting between images.

Values of $\tilde{Y}$ in the captured images are then averaged in the direction perpendicular to the flow. Subsequently, and being careful to consider only those images where the wetting front is yet to reach the end of the strip—so that the semi-infinite definition of eq. 2 holds—, we apply the transformation eq. 3. We verified that $\tilde{Y}$ values extracted from different images of each strip approximately coincide when expressed in terms of Boltzmann variable ϕ. This observed self-similarity serves as a further confirmation that eq. 2 can model the physical phenomenon under observation.

We repeated this processing step using the data from lateral flow in three different paper-based devices. We then combined the data from the three experiments, while allowing for a correction factor in ϕ to control for small differences in the overall speed of the imbibition across the different devices (Elizalde et al., 2016) while still capturing the overall shape of the water distribution profiles. In the final step we grouped the datapoints in 141 windows of $15\,\mu\text{ms}^{-1/2}$ in ϕ and used the averages from the three devices to compute the final observed values and standard deviations, the latter after being passed through a uniform filter spanning ten windows.

Experimental data–driven diffusivity reconstruction. The Bruce and Klute method was used to obtain an approximation of the diffusivity function $D(\theta)$ that would explain the experimental data. For this, the experimental average curve was passed through an isotonic regression (Chakravarti, 1989) and subsequently interpolated with a PCHIP (Fritsch and Carlson, 1980) monotonic spline to enable the evaluation of eq. 4.

3.2 Numerical solver and parameter estimation

Parameter estimation was performed by iteratively solving eq. 2 whilst varying the desired parameters, with the goal of obtaining the best fit to the experimental data as measured with least squares weighted by the uncertainties in the experimental data. Problems were solved with *Fronts* (Gerlero et al., 2020), a specialized numerical package able to find the required solutions to eq. 2 by taking advantage of the Boltzmann transformation.

The *BlackBoxOptim* (Feldt, 2019) package was used to find values for the unknown parameters by repeatedly invoking the solver and assessing the solutions. For this, a method of the differential evolution family was run in parallel. The optimization is configured to finish after 10 000 steps of the differential evolution algorithm, where each step will cause *Fronts* to be invoked at least once.

Exploiting the diffusive nature of the problem, parameters that are constant factors in D (e.g. K_s/α in Brooks and Corey and Van Genuchten, and D_{wt} in LETd) are not explored by the same optimizer. Instead, an intermediate optimization layer is introduced in the process that finds the best constant factor by scaling the solutions in ϕ, which can be done without additional solver calls.

Overall, the scheme turned out to be very efficient, with the entire process of fitting the parameters for the models we examined taking only between 10 and 40 minutes on a MacBook Pro (Apple Inc., Cupertino, Calif., USA) notebook computer equipped with a Core i7-3615QM (Intel Corporation, Santa Clara, Calif., USA) processor and 8 GB of system RAM.

After the optimizer finishes, values of the parameters are rounded to four significant figures for easier reporting and fed again to the solver before computing the reported value of the reduced chi-square (χ^2_ν) statistic (Taylor, 1997).

3.3 Estimation and propagation of uncertainties

MCMC for Bayesian Inference. To estimate the uncertainty in the parameters $\mathbf{x} \in \mathbb{R}^{Np}$, a Bayesian framework was employed. More specifically the Markov Chain Monte Carlo (MCMC) method (Brooks, 1998; Brooks et al., 2011) was used to compute the Bayes' rule,

$$\mathbb{P}(\mathbf{x}|D) = \frac{\mathbb{P}(D|\mathbf{x})\,\mathbb{P}(\mathbf{x})}{\mathbb{P}(D)}, \tag{8}$$

where for simplicity we consider $D := \theta^{exp}$ obtained from Equation 6. $\mathbb{P}(D) := \boldsymbol{\sigma}^{exp}$ is referred to as evidence quantifying the variability of the observed data D. $\mathbb{P}(\mathbf{x})$ represents the prior "knowledge" for each model parameter (independently from the data D). $\mathbb{P}(D|\mathbf{x})$ is the likelihood function (revealing the discrepancies between the observed data D and a function of the solution to eq. 2 evaluated in a fixed sample taken from the distribution of $\mathbf{x}$). Successive computations of eq. 8 result in a Markov chain that asymptotically converges to the kernel of the density distribution of the uncertain parameter $\mathbf{x}$ that best fit the data D, in other words $\mathbb{P}(\mathbf{x}|D)$. In this manuscript the MCMC was implemented using the Python library `PyMC3`, and adopting the `SLICE` sampler presented in the work of Salvatier et al. (2016).

Emulators vs. simulators. Surrogate models (or emulators) were employed to replace the simulator calls when the number of execution turns not feasible to be performed. In this work Polynomial Chaos Expansions (PCEs) (Nagel and Sudret, 2016; Gratiet et al., 2016) were tailored to obtain the same responses that a simulator can return. In general, PCE emulators map the parameters' uncertainty $\mathbb{P}(\mathbf{x}|D)$, to different Quantities of Interest (QoI) adopting a polynomial structure. For any output quantity $\mathcal{Y}$ the associated PCE emulator is written in terms of a truncated polynomial expansion, yielding the next definition:

$$\mathcal{Y}^{PC} := \sum_{i=0}^{N-1} \boldsymbol{\psi}_i(\mathbf{x})\, y_i, \tag{9}$$

where $\boldsymbol{\psi}_i(\mathbf{x})$ represents the orthonormal basis and $\mathcal{Y}^{PC}$ is the approximation of the random response of the QoI. The number of terms N considered in the expansion is a function of the number of uncertain inputs and the polynomial degree P_d given by $N = \frac{(N_p+P_d)!}{P_d!N_p!}$. The coordinates y_i that fix the polynomial expansion written in eq. 9 are obtained minimizing the difference between $\mathcal{Y}$ and $\mathcal{Y}^{PC}$. The uncertainty

quantification will be materialized in the evaluation of statistical moments like the expected value and variance of the QoI. They are computed as:

$$\mathbb{E}[\mathcal{Y}] := \int \mathcal{Y}\,\pi(\mathbf{x}) = y_0, \tag{10}$$

$$\mathbb{V}[\mathcal{Y}] := \int (\mathcal{Y} - \mathbb{E}[\mathcal{Y}])^2\ \pi(\mathbf{x}) = \sum_{i>0} {y_i}^2, \tag{11}$$

where $\pi(\mathbf{x}) = \prod_i^{N_p} \pi_i(x_i)$, and $\pi_i(x_i)$ is the marginal probability distribution functions (i.e. $\pi_i(x_i) := \mathbb{P}(x_i|D)$). The evaluation of expected value and variance results in simple polynomial operations.

Uncertainty decomposition. Global (variance based) Sensitivity analysis was used to assess how the input parameters $x_i \in \mathbf{x}$ and also interactions between them contribute to a particular output quantity $\mathcal{Y}$, adopting the Sobol sensitivity indices (Sobol, 2001; Saltelli et al., 2008). The first order Sobol index (also known as main Sobol index), expresses how a certain uncertain input x_i directly contributes to the variance of the output $\mathcal{Y}$. It is given by the following expression:

$$S_i := \frac{\mathbb{V}[\mathbb{E}[\mathcal{Y}|x_i]]}{\mathbb{V}[\mathcal{Y}]}. \tag{12}$$

The first order Sobol index neglects eventual interactions between two or more different uncertain inputs. To estimate the changes on $\mathbb{V}[\mathcal{Y}]$ considering first and high-order interactions of the *i-th* uncertain input, the total Sobol index (Saltelli et al., 2008) is used, which is given by:

$$S_{Ti} := 1 - \frac{\mathbb{V}[\mathbb{E}[\mathcal{Y}|x_{-i}]]}{\mathbb{V}[\mathcal{Y}]}, \tag{13}$$

where x_{-i} denotes the set of all inputs except x_i.

In this paper, the computational implementation of the PCE emulators was performed using the Python library `ChaosPy` presented in the work of Feinberg and Langtangen (2015).

4 Results and discussion

4.1 Experimental results

Initial moisture content. From the oven-drying experiments, we were able to estimate the air-dry volumetric moisture content θ_i of Whatman No. 1 paper at 0.025±0.002. The stability of the obtained results was verified for θ_i within the reported range of uncertainty (0.023–0.027). We note that, in the absence of this consideration, an initial condition of $\theta = 0$ would appear to be a sensible assumption. However, with all of the hydraulic models under study, this condition will result in zero diffusivity and therefore no flow in the domain, a fact that is obviously unrealistic—unless one also accepts negative values for θ_r or S_{wir}, which is unconventional, or is willing to introduce other assumptions (Rath et al., 2018). By measuring the actual moisture content in air-dry condition, we do not require any of these workarounds.

Porosity. By comparing the initial (air-dry) and saturated weights of the paper-based devices, we measured a porosity of 0.70 ± 0.06. The general methodology of this measurement and its result are in line with those reported by others (Rath et al., 2018; Cummins et al., 2017) for Whatman No. 1 paper, and we will therefore adopt the value $\theta_s = 0.7$.

Lateral flow wetting profile. Experimental data were processed as previously described. Intermediate and final results of data processing appear in Figure 2. Figure 2**A** shows the intensity profiles at different times for a single device. Figure 2**B** displays the final results in water content versus the Boltzmann variable, plotting the average across the three devices and the standard deviation. The observed self-similarity of profiles at different times is subsequently reflected in the low standard deviations along the final profile.

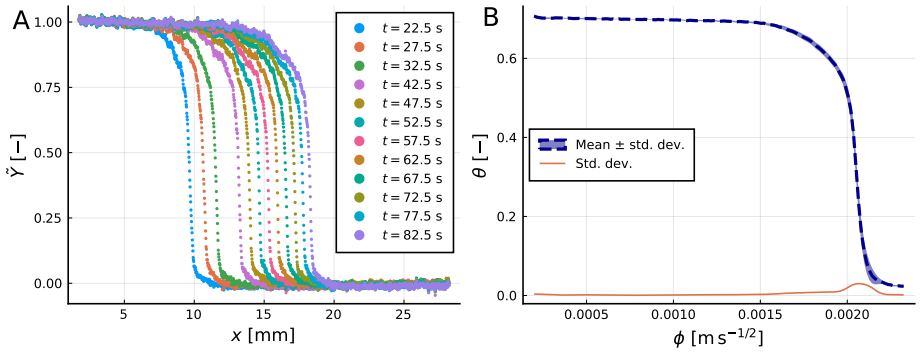

Fig. 2 **A** Intermediate results of data processing in a single paper-based device. **B** Final results of data processing (average water content and standard deviation, expressed in the Boltzmann variable). The low values of standard deviations are a consequence of the self-similarity of the profiles taken at different times.

Parameter estimation. With the experimental wetting profile as the objective, we ran our parameter estimation study to find the best fits that can be obtained with each of the candidate models. These results are reported in Table 1 and in Figures 3 and 4. The figures show, respectively, the wetting profiles and diffusivity functions of the different fitted models compared to the experimental data.

From Figure 3 it is straightforward to infer that the Brooks and Corey model was unable to match the experimental curve, while the Van Genuchten model is able to reproduce most of the expected profile—but the approximation breaks down with a sharp corner at the transition to initial conditions. In contrast, the LET-based models—both the one based on existing LET correlations as well as our own LETd function with fewer parameters—can approximate the experimental profile very closely at all points.

The reduced chi-square values shown in Table 1 confirm that Brooks and Corey model is not acceptable, and that LET models yield results that are somewhat better than those obtained with the Van Genuchten model.

The comparison of the diffusivity functions $D(\theta)$ obtained for each model is presented in Figure 4. These results verify the observations made in Figure 3, i.e. the LET-based models appear to be better match the reconstructed $D(\theta)$ in the entire domain of θ. For its part, the Brooks and Corey model only matches the curve twice, and the Van Genuchten model increasingly strays from the experimental $D(\theta)$ as θ goes below 0.4. Analyzing these results, we find it remarkable how LET-based models are able to reproduce $D(\theta)$ well across its whole range of validity. It is also important to note that the differences between the LETx + LETs and LETd models are minor, demonstrating the validity of the considerations made when proposing the LETd model. In light of this, for further analysis we will disregard the LETx + LETs model and consider only LETd, which uses three fewer parameters. Additionally, we used the four obtained $D(\theta)$ functions to predict the flow velocity profiles at different times. The smoothness of the LETd velocity curves should make this model is better posed for coupled scalar transport models with convection–diffusion–reaction equations. These results are reported in the supporting information.

Table 1 Final results of parameter estimation using *Fronts* and the experimental data.

Model	Parameters		χ^2_ν
Brooks and Corey	n	0.2837	691
	l	4.795	
	θ_r	2.378×10^{-5}	
	K_s/α	$3.983 \times 10^{-6}\,\mathrm{m^2\,s^{-1}}$	
Van Genuchten	n	8.093	1.7
	l	2.344	
	θ_r	0.004 943	
	K_s/α	$2.079 \times 10^{-6}\,\mathrm{m^2\,s^{-1}}$	
LETx + LETs	L_w	1.651	1.0
	E_w	230.5	
	T_w	0.9115	
	L_s	0.517	
	E_s	493.6	
	T_s	0.3806	
	S_{wir}	0.016 80	
	$K_s P_{cir}/\gamma$	$8.900 \times 10^{-3}\,\mathrm{m^2\,s^{-1}}$	
LETd	L	0.004 569	1.5
	E	12 930	
	T	1.505	
	S_{wir}	0.028 36	
	D_{wt}	$4.660 \times 10^{-4}\,\mathrm{m^2\,s^{-1}}$	

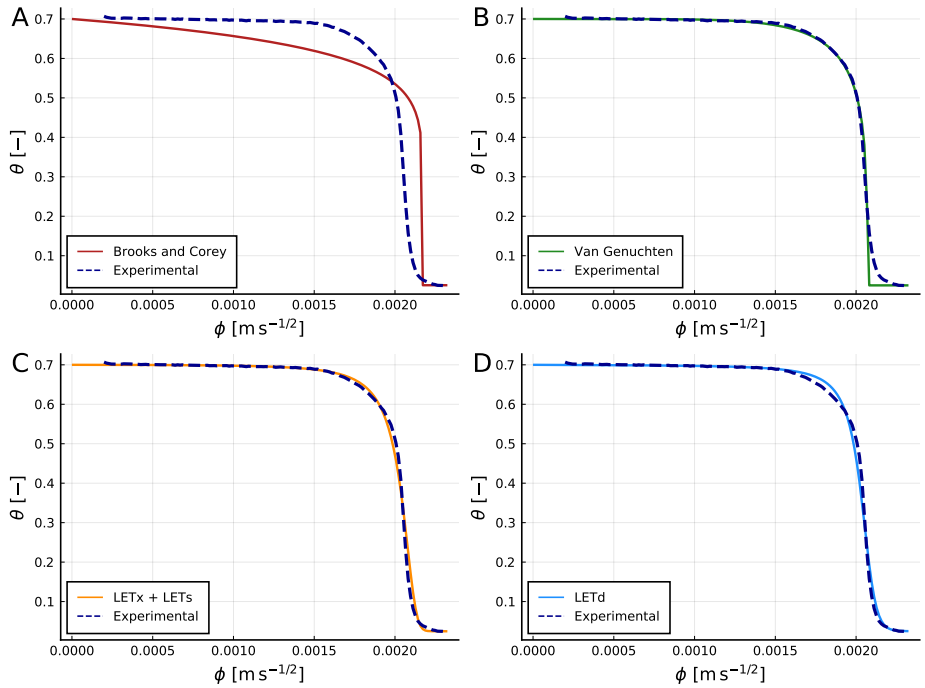

Fig. 3 Best fits of the imbibition profiles represented with the Boltzmann variable for the different models considered in this work.

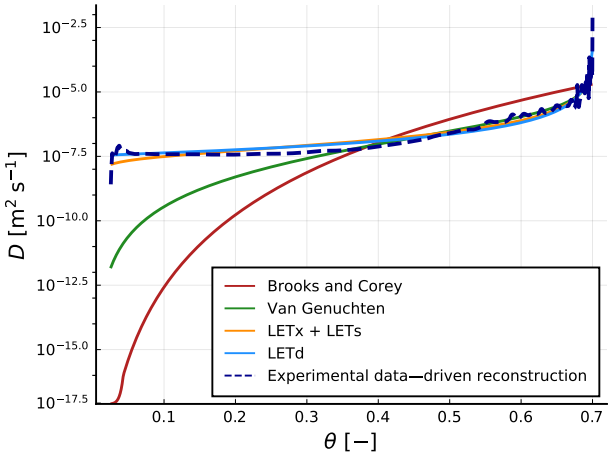

Fig. 4 Comparison of the experimental reconstructed $D(\theta)$ and the diffusivities of the different models with the best fit parameters.

Finally, in order to demonstrate the applicability of these results in the design and manufacturing of paper-based microfluidic devices, we perform a cross validation experiment on different geometries (Tirapu-Azpiroz et al., 2018). We constructed different numerical prototypes based on OpenFOAM® (Horgue et al., 2015) using the model parameter sets reported in Table 1. These numerical prototypes were compared with the experimental results obtained for each geometry. Details and results of this validation step can be found in the supporting information.

4.2 Model adjustment considering uncertainty in observed data

Each diffusion model contains parameters with (and without) an associated physical meaning. The uncertain response of the diffusion models is analyzed considering variability on the parameters without physical meaning. In a more general case, we are interested in exposing the difficulties to obtain unique values for the parameters n and l for the Brooks and Corey, and Van Genuchten models. As well as the L, E, T tuple for the LETd model. Taking into account the experimental variability, the MCMC was executed adopting uniform priors for each uncertain input. These uniform priors were upper and lower bounded taking the best fit values reported in Table 1 allowing total variations of 70% with respect to their nominal value. The execution of the MCMC provided a 20000-long Markov chain for each uncertain parameter. The kernel density estimates are shown in Figures 5, 6, and 7, for the Brooks and Corey, Van Genuchten and LETd models, respectively. The density distribution associated to the Brooks and Corey model presented for both non-physical parameters multi-modal shapes revealing the strong limitations of the model to determine a unique stable pair of n and l, that best fits the experimental data. In particular, we can note that the best fit values reported in Table 1 have a very small frequency for the n parameter and its rejected in the l density estimate, as shown in Figure 5.

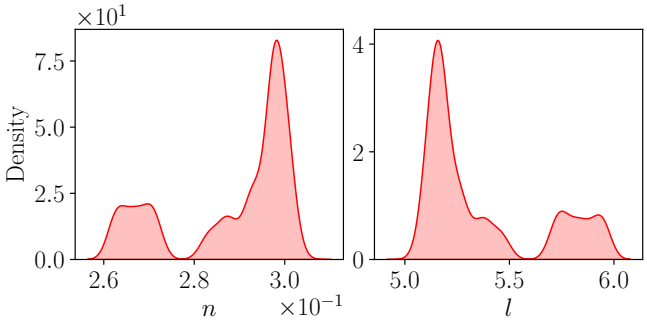

Fig. 5 Posterior distributions for each *Brooks and Corey* non-physical parameters.

The Van Genuchten model presented a mixture of density distribution functions, n has a more symmetric distribution than the l parameter. In both cases the best fit values reported in Table 1 were excluded from the posterior density

estimates as depicted in Figure 6. In both cases, the best fit rejection, suggests that the there are many other local minimums that satisfies the fitting requests.

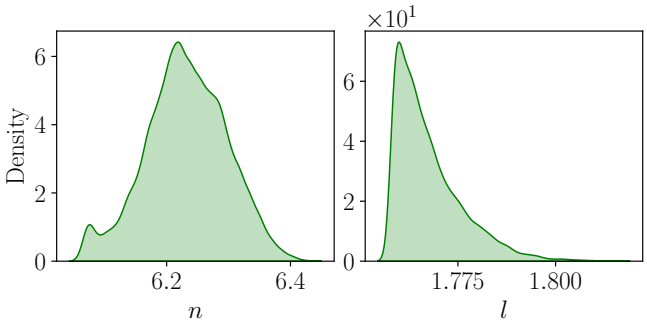

Fig. 6 Posterior distributions for each *Van Genuchten* non-physical parameters.

The samples obtained from the Markov chains considering the LETd model presented asymmetric shapes for the three parameters, and exposed multi-modal density distributions for the E and T parameters. In Figure 7 the LETd model reduces the probability to recover the best fit value shown in Table 1 only for the L parameter, while (in contrast to the previous models) for parameters E and T best fit values are contained by the density distributions.

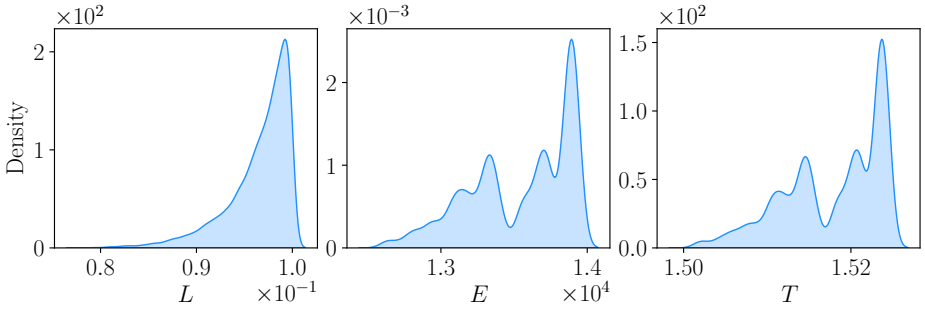

Fig. 7 Posterior distributions for each *LETd* non-physical parameters.

4.3 Effects of uncertainties in QoIs

Here, the QoI studied was the $L^2(\Omega)$ error between the experimental observation and the numerical model evaluation performed with *Fronts*, i.e.:

$$L^2(\Omega) = \|\theta^{exp}(\phi) - \theta(\phi)\|_2. \tag{14}$$

We performed a similar analysis for the absolute error between the experimental observation and the *Fronts* model evaluation, employing the three diffusion models.

However, the results are not included here, since they are equivalent to the findings exposed for the $L^2(\Omega)$ error.

The QoI was chosen to evaluate the capabilities of different hydraulic models to reproduce the experimental imbibition fronts in paper substrates. As expected, if a model evaluation returns values near zero for the QoI means that such model have a good capability to recover the experimental observation. Whereas, non-negligible values for the QoI, exposes its limitations. In this manuscript, the PCE emulators were calibrated considering third order polynomials for the Brooks and Corey and Van Genuchten models and a second order polynomial for the LETd model. Additionally, the emulators were adjusted with 300 successful deterministic evaluations. These PCE settings ensure that the error between the simulators and the emulators are small enough to use the emulators. During the calibration of the PCE emulators several failures happened when solving eq. 2 by drawing samples from the MCMC posterior density distributions. The LETd model had a degree of success of 100%, the Van Genuchten reported an 88% success rate, and the Brooks and Corey had a 43% rate of success. In this context, the LETd model demanded 300 model evaluations to fit the PCE. Whereas, the Van Genuchten and the Brooks and Corey models requested 340 and 693 deterministic evaluations to fit the PCE emulators, respectively.

Figure 8 shows the estimated uncertainty for each model analyzing the $L^2(\Omega)$ error. The kernel distribution estimate for the analyzed QoI reveals the same non-symmetric and proper shapes for the Brooks and Corey and LETd models certifying that the error estimates are always upper bounded with an abrupt lower threshold. In particular, the Brooks and Corey model had inferior quality response in terms of accuracy and uncertainty propagation. Whereas, the LETd model had better performance in terms of accuracy and uncertainty propagation; the Van Genuchten model presented $L^2(\Omega)$ errors clustered around a unique value revealing almost no uncertain behavior. Yet, the error values where clustered near the worst cases that the LETd model can achieve. In addition to this, the estimated uncertainty adopting the Van Genuchten model shows a sharp upper-bound with a smooth decay towards smaller values of the $L^2(\Omega)$. This fact exposes that the parametric uncertainty shifted the best fit settings mentioned in Table 1 to a different minimal configuration.

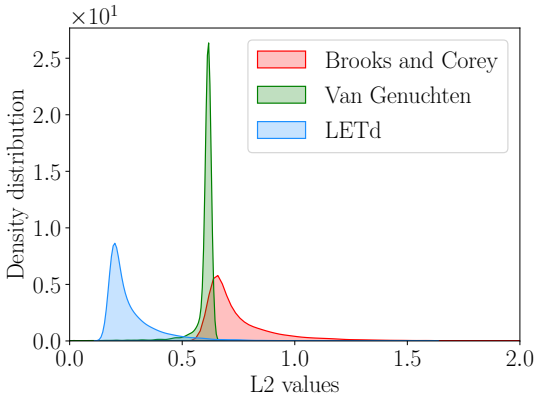

Fig. 8 Comparison between the uncertain response of *Fronts*, considering the Brooks and Corey, Van Genuchten and LETd models with the experimental data

The Table 2 shows the Sobol indices analyzing the variability of the $L^2(\Omega)$ error, considering the non-physical parameters of each diffusion model. The Brooks and Corey sensitivity analysis states clearly that the variability of the QoI can be reduced by only improving the estimation of the l parameter. A similar sensitivity pattern is recognized on the Van Genuchten Sobol indices. Although the $L^2(\Omega)$ error has small variability adopting the Van Genuchten diffusion model, the Sobol indices reveals that variance reductions are exclusively conditioned to improving the estimation of l. In the case of the LETd model, the $L^2(\Omega)$ variability can be reduced minimizing the fluctuations of the E and T parameters. Moreover, the LETd model presents interactions between the parameters E and T, constraining the variability reduction to appropriate results of E and T.

Table 2 Sensitivity analysis results considering the three diffusion models.

Sobol index	Brooks and Corey		Van Genuchten		LETd		
Main	$n : 1.29 \times 10^{-3}$	$l : 9.96 \times 10^{-1}$	$n : 7.03 \times 10^{-17}$	$l : 1.00$	$L : 1.97 \times 10^{-5}$	$E : 7.76 \times 10^{-1}$	$T : 2.23 \times 10^{-1}$
Total	$n : 3.26 \times 10^{-3}$	$l : 9.98 \times 10^{-1}$	$n : 3.83 \times 10^{-11}$	$l : 1.00$	$L : 2.19 \times 10^{-3}$	$E : 7.75 \times 10^{-1}$	$T : 7.14 \times 10^{-1}$

5 Summary and Conclusions

An objective testing and a discussion about the suitability of different contemporary $D(\theta)$ models for representing fluid flow dynamics in paper substrates was presented. We obtain experimental data from carefully designed lateral flow experiments in Whatman #1 paper. The extent and quality of these measurements are evidenced by the excellent results in self-similarity of the profiles, with a very low standard deviation obtained for all the collected data. We reproduced those experimental fluid fronts with the best parameter fits of the models showing the limitations and capabilities of each model to represent the moisture content function $\theta(\phi)$. We used the *Fronts* solver, which showed remarkable efficiency in solving

eq. 2: over ten thousand invocations for model fitting and twenty thousand invocations for uncertainty quantification, for each model, in less than an hour of total computing time.

Additionally, we presented an adapted model targeted to paper-based microfluidic applications based on LET model, with a reduced number of parameters yet still showing an excellent performance in terms of accuracy and robustness. We demonstrated the favorable characteristics of the LETd model through a data-driven reconstruction of $D(\theta)$ and its comparison with different models. From this study, we conclude that the simplifications made to obtain the LETd model from the original LET-based models do not affect the ability to accurately represent the experimental $D(\theta)$ in the whole domain of θ. This situation cannot be reproduced with the Van Genuchten model for $\theta > 0.4$, nor with the Brooks and Corey model for almost the entire domain of θ. Additional studies were performed with different geometries in order to confirm the validity of the reported model parameters beyond lateral flow, yet also establishing the suitability of the LET-based models to adequately model both fluid front profiles and flow velocity profiles.

An analysis on the propagation of uncertainties allowed us to characterize the robustness of the models for representing the experimental data under different experimental conditions. With the exception of E and T, all deterministic best fit parameters obtained with *Fronts* were not included into the different density distribution associated to the models. Additionally, non-trivial uncertainty propagation was found only with the LETd model. These facts reflect the lack of robustness of the classical models under variations of the experimental data. In other words, when using classical models to fit experimental imbibition data, a small variation of the measured values will produce completely different tuples of ideal parameters, and maybe several of them will show similar fit performances.

Finally, after the presented analysis, it is possible to confirm that LETd model can effectively represent fluid flow imbibition front in the whole range of θ, yielding more robust and reproducible results than classical models when complex contemporary paper-based microfluidic devices are studied.

Declarations

Funding

This research was supported by CONICET, ANPCyT (Grant PICT 2018-02920), UTN (Grant PID ASUTNFE0005525) UNL(Grant CAI+D 50620190100114LI), Argentina and by the Coordenação de Aperfeiçoamento de Pessoal de Nível Superior - Brasil (CAPES) - Finance Code 001.

Conflict of interest

All authors declare complete absence of financial/commercial conflicts of interest.

Data availability

The datasets generated during and/or analysed during the current study are available from the corresponding author on reasonable request.

Supporting information

Supporting information providing formal hypothesis and mathematical definitions for different hydraulic models, as well as results of validation experiments and numerical simulations using the obtained parameter sets on different geometries, can be found in the on-line version of the article.

References

Bear J, Cheng AHD (2010) Modeling groundwater flow and contaminant transport, vol 23. Springer Science & Business Media, Dordrecht, Netherlands

Berli CLA, Kler PA (2016) A quantitative model for lateral flow assays. Microfluidics and Nanofluidics 20(7):104

Boltzmann L (1894) Zur Integration der Diffusionsgleichung bei variabeln Diffusionscoefficienten (to integrate the diffusion equation with variable diffusion coefficients). Annalen der Physik 289(13):959–964

Brooks R, Corey T (1964) Hydraulic properties of porous media. Hydrology Papers, Colorado State University 24:37

Brooks S (1998) Markov chain Monte Carlo method and its application. Journal of the royal statistical society: series D (the Statistician) 47(1):69–100

Brooks S, Gelman A, Jones G, Meng X (2011) Handbook of Markov chain monte carlo. CRC press

Bruce R, Klute A (1956) The measurement of soil moisture diffusivity. Soil Science Society of America Journal 20(4):458–462

Chakravarti N (1989) Isotonic median regression: a linear programming approach. Mathematics of operations research 14(2):303–308

Cummins BM, Chinthapatla R, Ligler FS, Walker GM (2017) Time-dependent model for fluid flow in porous materials with multiple pore sizes. Analytical Chemistry 89(8):4377–4381

Das S, Mitra SK (2013) Different regimes in vertical capillary filling. Physical Review E 87(6):063005

Das S, Waghmare PR, Mitra SK (2012) Early regimes of capillary filling. Physical Review E 86(6):067301

Elizalde E, Urteaga R, Berli CLA (2016) Precise capillary flow for paper-based viscometry. Microfluidics and Nanofluidics 20(10):1–8

Espejo A, Giráldez JV, Vanderlinden K, Taguas E, Pedrera A (2014) A method for estimating soil water diffusivity from moisture profiles and its application across an experimental catchment. Journal of Hydrology 516:161–168

Evangelides C, Tzimopoulos C, Arampatzis G (2005) Flux-saturation relationship for unsaturated horizontal flow. Soil science 170(9):671–679

Evangelides C, Arampatzis G, Tzimopoulos C (2010) Estimation of soil moisture profile and diffusivity using simple laboratory procedures. Soil science 175(3):118–127

Feinberg J, Langtangen HP (2015) Chaospy: An open source tool for designing methods of uncertainty quantification. Journal of Computational Science 11:46–57

Feldt R (2019) BlackBoxOptim.jl. https://github.com/robertfeldt/BlackBoxOptim.jl

Franck N, Schaumburg F, Kler PA, Urteaga R (2021) Precise electroosmotic flow measurements on paper substrates. Electrophoresis 42(7-8):975–982

Fritsch FN, Carlson RE (1980) Monotone piecewise cubic interpolation. SIAM Journal on Numerical Analysis 17(2):238–246

Gamazo P, Slooten LJ, Carrera J, Saaltink MW, Bea S, Soler J (2016) Proost: object-oriented approach to multiphase reactive transport modeling in porous media. Journal of Hydroinformatics 18(2):310–328

Gerlero GS, Kler PA, Berli CLA (2020) Fronts.jl. https://github.com/gerlero/Fronts.jl

Gerlero GS, Márquez Damián S, Schaumburg F, Franck N, Kler PA (2021) Numerical simulations of paper-based electrophoretic separations with open-source tools. Electrophoresis 42:1543–1551

Gratiet LL, Marelli S, Sudret B (2016) Metamodel-based sensitivity analysis: polynomial chaos expansions and gaussian processes. Handbook of Uncertainty Quantification pp 1–37

Hassan Su, Tariq A, Noreen Z, Donia A, Zaidi SZ, Bokhari H, Zhang X (2020) Capillary-driven flow microfluidics combined with smartphone detection: An emerging tool for point-of-care diagnostics. Diagnostics 10(8):509

Hertaeg MJ, Tabor RF, Berry JD, Garnier G (2020) Radial wicking of biological fluids in paper. Langmuir 36(28):8209–8217

Hong S, Kim W (2015) Dynamics of water imbibition through paper channels with wax boundaries. Microfluidics and Nanofluidics 19(4):845–853

Horgue P, Soulaine C, Franc J, Guibert R, Debenest G (2015) An open-source toolbox for multiphase flow in porous media. Computer Physics Communications 187:217–226

Kim TH, Hahn YK, Kim MS (2020) Recent advances of fluid manipulation technologies in microfluidic paper-based analytical devices (μpads) toward multi-step assays. Micromachines 11(3):269

Lim H, Jafry AT, Lee J (2019) Fabrication, flow control, and applications of microfluidic paper-based analytical devices. Molecules 24(16):2869

Lomeland F (2018) Overview of the LET family of versatile correlations for flow functions. In: Proceedings of the International Symposium of the Society of Core Analysts, pp SCA2018–056

Lomeland F, Ebeltoft E (2008) A new versatile capillary pressure correlation. In: Proceedings of the International Symposium of the Society of Core Analysts, vol 29, pp SCA2008–08

Lomeland F, Ebeltoft E, Thomas WH (2005) A new versatile relative permeability correlation. In: Proceedings of the International Symposium of the Society of Core Analysts, vol 112, pp SCA2005–32

Modha S, Castro C, Tsutsui H (2021) Recent developments in flow modeling and fluid control for paper-based microfluidic biosensors. Biosensors and Bioelec-

tronics p 113026
Mora MF, Garcia CD, Schaumburg F, Kler PA, Berli CL, Hashimoto M, Carrilho E (2019) Patterning and modeling three-dimensional microfluidic devices fabricated on a single sheet of paper. Analytical chemistry 91(13):8298–8303
Nagel J, Sudret B (2016) Spectral likelihood expansions for bayesian inference. Journal of Computational Physics 309:267–294
Ozer T, McMahon C, Henry CS (2020) Advances in paper-based analytical devices. Annual Review of Analytical Chemistry 13:85–109
Pan B, Clarkson CR, Atwa M, Tong X, Debuhr C, Ghanizadeh A, Birss VI (2021) Spontaneous imbibition dynamics of liquids in partially-wet nanoporous media: Experiment and theory. Transport in Porous Media 137(3):555–574
Perez-Cruz A, Stiharu I, Dominguez-Gonzalez A (2017) Two-dimensional model of imbibition into paper-based networks using Richards' equation. Microfluidics and Nanofluidics 21(5):98
Philip J (1955) Numerical solution of equations of the diffusion type with diffusivity concentration-dependent. Transactions of the Faraday Society 51:885–892
Rath D, Toley BJ (2020) Modeling-guided design of paper microfluidic networks: A case study of sequential fluid delivery. ACS sensors
Rath D, Sathishkumar N, Toley BJ (2018) Experimental measurement of parameters governing flow rates and partial saturation in paper-based microfluidic devices. Langmuir 34(30):8758–8766
Richards LA (1931) Capillary conduction of liquids through porous mediums. Physics 1(5):318–333
Ruoff AL, Prince DL, Giddings JC, Stewart GH (1959) The diffusion analogy for solvent flow in paper. Kolloid-Zeitschrift 166(2):144–151
Ruoff AL, Stewart GH, Shin HK, Giddings JC (1960) Diffusion of liquids in unsaturated paper. Kolloid-Zeitschrift 173(1):14
Salentijn GI, Grajewski M, Verpoorte E (2018) Reinventing (bio) chemical analysis with paper. Anal Chem 90(23):13815–13825
Saltelli A, Ratto M, Andres T, Campolongo F, Cariboni J, Gatelli D, Saisana M, Tarantola S (2008) Global sensitivity analysis. The primer, vol 304. John Wiley & Sons Ltd.
Salvatier J, Wiecki T, Fonnesbeck C (2016) Probabilistic programming in python using pymc3. PeerJ Computer Science 2:e55
Santagata T, Solimene R, Aprea G, Salatino P (2020) Modelling and experimental characterization of unsaturated flow in absorbent and swelling porous media: Material characterization. Transport in Porous Media 134(3):725–753
Schaumburg F, Berli CLA (2019) Assessing the rapid flow in multilayer paper-based microfluidic devices. Microfluidics and Nanofluidics 23(8):98
Schaumburg F, Kler PA, Berli CLA (2018a) Numerical prototyping of lateral flow biosensors. Sensors and Actuators B: Chemical 259:1099–1107
Schaumburg F, Urteaga R, Kler PA, Berli CLA (2018b) Design keys for paper-based concentration gradient generators. Journal of Chromatography A 1561:83–91
Sobol I (2001) Global sensitivity indices for nonlinear mathematical models and their Monte Carlo estimates. Mathematics and computers in simulation 55(1-3):271–280
Taylor J (1997) Introduction to error analysis, the study of uncertainties in physical measurements

Terzis A, Yang G, Zarikos I, Elizalde E, Weigand B, Kalfas A, Ding X (2018) A temperature-based diagnostic approach for paper-based microfluidics. Microfluidics and Nanofluidics 22(3):1–6

Tirapu-Azpiroz J, Silva AF, Ferreira ME, Candela WFL, Bryant PW, Ohta RL, Engel M, Steiner MB (2018) Modeling fluid transport in two-dimensional paper networks. Journal of Micro/Nanolithography, MEMS, and MOEMS 17(2):025003

Tumidajski PJ, Chan GW (1996) Boltzmann-Matano analysis of chloride diffusion into blended cement concrete. Journal of Materials in Civil Engineering 8(4):195–200

Urteaga R, Elizalde E, Berli CLA (2018) Transverse solute dispersion in microfluidic paper-based analytical devices (μPADs). Analyst 143(10):2259–2266

Urteaga R, Mercuri M, Gimenez R, Bellino MG, Berli CL (2019) Spontaneous water adsorption-desorption oscillations in mesoporous thin films. Journal of colloid and interface science 537:407–413

Van Genuchten MT (1980) A closed-form equation for predicting the hydraulic conductivity of unsaturated soils. Soil Science Society of America journal 44(5):892–898

Vincent O, Marguet B, Stroock AD (2017) Imbibition triggered by capillary condensation in nanopores. Langmuir 33(7):1655–1661

Yamada K, Shibata H, Suzuki K, Citterio D (2017) Toward practical application of paper-based microfluidics for medical diagnostics: state-of-the-art and challenges. Lab on a Chip 17(7):1206–1249

Yetisen AK, Akram MS, Lowe CR (2013) Paper-based microfluidic point-of-care diagnostic devices. Lab on a Chip 13(12):2210–2251